

Time-delayed feedback control of shear-driven micellar systems

Benjamin von Lospichl* and Sabine H. L. Klapp†
*Institut für Theoretische Physik, Sekretariat EW 7-1,
Technische Universität Berlin,
Hardenbergstraße 36, D-10623 Berlin, Germany*

(Dated: July 3, 2019)

Suspensions of elongated micelles under shear display complex non-linear behaviour including shear banding, spatio-temporal oscillatory patterns and chaotic response. Based on a suitable rheological model [S. M. Fielding and P. D. Olmsted, *Phys. Rev. Lett.* **92**, 084502 (2004)], we here explore possibilities to manipulate the dynamical behaviour via closed-loop (feedback) control involving a time delay τ . The model considered relates the viscoelastic stress of the system to a structural variable, that is, the length of the micelles, yielding two time- and space-dependent dynamical variables ξ_1, ξ_2 . As a starting point we perform a systematic linear stability analysis of the uncontrolled system for (i) an externally imposed average shear rate and (ii) an imposed total stress, and compare the results to those from extensive numerical simulations. We then apply the so-called Pyragas feedback scheme where the evolution equations for one or both variables are supplemented by a control term of the form $K(\xi_i(t) - \xi_i(t - \tau))$. Focusing on parameters close to a Hopf bifurcation, where the uncontrolled systems display oscillatory or chaotic states, we demonstrate that the Pyragas control can stabilize homogeneous steady states for both types of control. We explore in detail the regimes of successful stabilization in the K - τ -plane by a linear stability analysis and by simulations. It turns out that the results from the (simpler) diagonal Pyragas scheme, which acts on both variables, are quite close to those from the physically more meaningful non-diagonal scheme acting on the stress alone.

PACS numbers: 47.57.Qk, 05.45.Gg, 47.52.+j, 02.30.Yy

I. INTRODUCTION

Exposing soft matter systems to shear flow often results in a non-linear behavior of measurable rheological quantities (such as viscosity, stress) and to instabilities. The most prominent example is the shear banding instability, where the system splits into two or multiple spatial regions (“bands”) of different local shear rate and local viscosity [1–4]. This instability is indicated by a non-monotonicity of the flow curve, that is, the relationship between the total stress T in the steady state and the imposed shear rate $\dot{\gamma}$. Shear banding occurs in many complex fluids like polymer solutions, emulsions or liquid crystals. To capture this phenomenon theoretically, several non-linear models have been proposed revealing multiple branches of the underlying constitutive curve $T(\dot{\gamma})$. A classical example is the diffusive Johnson-Segalman model [1, 5].

In the present article we concentrate on one of the most prominent examples of a shear-banding system, namely solutions of elongated or wormlike micelles. Within the past decades the self-assembly processes as well as the rheological properties of such systems have attracted a lot of interest [6–9]. Due to their flexibility, on the one hand, and their ability to break and reform, on the other hand, wormlike micelles often called “living polymers”.

Further, wormlike micellar solutions exhibit an unique viscoelastic behaviour which can be exploited for many applications such as daily care products [10] or as fracturing fluids in oil recovery [11]. Indeed, already the first rheological experiments done by Rehage and co-workers demonstrated that the viscosity of these elongated micelles reveals a highly non-linear flow behaviour [12, 13]: Unlike covalently bound polymers, wormlike micelles can not only break but also recombine after exposing them to high shear forces. The first theory to account for the resulting viscoelastic spectra of wormlike micelles has been proposed by Turner and Cates [14, 15].

Beyond stationary shear bands and nonlinear viscosity, wormlike micellar solutions can moreover display oscillatory states and irregular or even chaotic spatio-temporal patterns, as indicated based on a bunch of experimental data based on particle image velocimetry and bulk-rheology [16–19]. Theoretical approaches to account for this complex behavior in micellar (and other complex) fluids may be subdivided into three classes. The first are spatially homogeneous models for the rheological (mechanical) dynamical variables such as T (or the viscoelastic stress σ) and $\dot{\gamma}$; this approach has been applied to shear-thickening fluids [20, 21]. The same variables are also at the center of several inhomogeneous or non-local models for shear-thinning [22, 23] and shear-thickening fluids [24]. These models additionally take into account that the macroscopic rheological behaviour is coupled to an intrinsic (microscopic) variable such as the polymer concentration [22], the micellar length [23], or the director of orientational ordering. The third class focuses

* blospichl@itp.tu-berlin.de

† klapp@physik.tu-berlin.de

directly on the (spatio-temporal) dynamics of liquid-crystalline substances, involving evolution equations for the (tensorial) nematic order parameter and its backcoupling to the flow [25–28].

The present study starts from a (non-local) model for micellar solutions proposed by Fielding and Olmsted [23], where the viscoelastic stress $\sigma(y, t)$ is coupled to the length $n(y, t)$ of the elongated micelles. This coupling of a mechanical and a structural variables destabilizes the high shear rate branch of the flow curve, giving rise to spatio-temporal oscillatory and chaotic solutions beyond a Hopf bifurcation [23]. The goal of the present paper is twofold: First, we systematically examine the system’s dynamics by a linear stability analysis for two rheological protocols (fixed average $\dot{\gamma}$ or T), thereby extending the results presented in Ref. [23]. Second, we explore methods to manipulate the occurring dynamical states by using time-delayed feedback control.

Indeed, in many technical applications of wormlike micelles the occurrence of oscillatory or chaotic states is not desired. Motivated by this, we here seek to stabilize *stationary* states inside the parameter range where the uncontrolled system displays oscillations. Specifically, we apply the concept of time-delayed feedback control (TDFC) as proposed by Pyragas in 1992 [29]. Within the Pyragas control scheme, the dynamical equations for the two variables ($\xi_1, \xi_2 = \sigma, n$) are supplemented by (local) control terms involving the difference $\xi_i(y, t) - \xi_i(y, t - \tau)$, with τ being the delay time. This type of control is *non-invasive* as the control forces vanish when the steady state (or a periodic state with period $T_{\text{osc}} = m\tau$ with $m = 1, 2, \dots$) is reached. The Pyragas scheme has been applied to a broad variety of non-linear systems from various fields (see [30, 31] for overviews) including semiconductor nanostructures, lasers, neural systems and general reaction-diffusion systems [32, 33]. There are also recent applications to the flow of soft-matter systems, both from the experimental [34] and from the theoretical side [35], an example being the stabilization of steady shear-aligned states in sheared liquid crystals [36]. Within the present study of micellar systems, we explore two routes of controlling the dynamical variables of our system: a “diagonal” scheme acting on both dynamical variables (σ and n) and a non-diagonal control scheme acting on σ alone. The latter is somewhat more involved from the theoretical side, but seems physically more meaningful in view of the experimental difficulties to measure $n(y, t)$.

Our publication is structured as follows. In Sec. II we review the model equations proposed in Ref. [23]. In Sec. III we describe the linear stability analysis for the two rheological protocols and compare the results with those from extensive numerical calculations of the full system. In Sec. IV we introduce the two routes of time-delayed feedback control. We then use the results of linear stability analysis derived in Sec III to find the neutral stability curves determining the parameter ranges where the control scheme is successful. The article closes with a brief summary and outlook.

II. MODEL EQUATIONS AND BACKGROUND

A. Flow geometry and force balance equation

We assume our micellar system to be subject to a planar Couette geometry consisting of two plates separated by a distance L along the y -direction. The lower plate is fixed at the position $y = 0$, while the upper plate located at the distance $y = L$ moves with a constant velocity in x -direction. This is equivalent to an externally imposed velocity field $\mathbf{v}^0 = v_x^0(y, t) \hat{\mathbf{x}}$, with $\hat{\mathbf{x}}$ being the unit vector in x -direction and $v_x^0(y, t) = y \bar{\gamma}(t)$. Here, $\bar{\gamma}(t)$ is the external shear rate corresponding to \mathbf{v}^0 . The *local* shear rate can be defined as spatial gradient of the actual velocity profile $v_x(y, t)$ in the system (which may differ from $v_x^0(y, t)$), that is, $\dot{\gamma}(y, t) = \partial_y v_x(y, t)$. In general, the total stress tensor \mathbf{T} of a viscoelastic fluid is defined by [37]

$$\mathbf{T} = \boldsymbol{\sigma} + 2\eta \mathbf{D} - p \mathbf{I}, \quad (1)$$

where $\boldsymbol{\sigma}$ is the viscoelastic contribution which may be related to a structural quantity. The second term on the r.h.s. of Eq. (1) denotes the Newtonian part, with η being the Newtonian viscosity and $2\mathbf{D} = \nabla \mathbf{v} + (\nabla \mathbf{v})^T$ the deformation tensor. The third term in Eq. (1) is an isotropic contribution, where p is the hydrostatic pressure and \mathbf{I} the identity matrix.

The dynamics of a viscoelastic fluid can be described through the generalized Navier-Stokes equation (or momentum balance equation)

$$\begin{aligned} \rho \left(\partial_t + \mathbf{v} \cdot \nabla \right) \mathbf{v} &= \nabla \cdot \mathbf{T} \\ &= \nabla \cdot \left(\boldsymbol{\sigma} + 2\eta \mathbf{D} - p \mathbf{I} \right), \end{aligned} \quad (2)$$

where ρ is the fluid density. We assume our system to be incompressible, i.e. $\nabla \cdot \mathbf{v} = 0$. Additionally, the system is assumed to be overdamped (limit of low Reynolds numbers). In this case the momentum balance equation (2) reduces to the force balance equation

$$\nabla \cdot \left(\boldsymbol{\sigma} + 2\eta \mathbf{D} - p \mathbf{I} \right) = 0. \quad (3)$$

For the present flow geometry and the imposed linear velocity field Eq. (3) reduces to

$$\partial_y \left(\sigma(y, t) + \eta \dot{\gamma}(y, t) \right) = 0, \quad (4)$$

where $\sigma(y, t)$ is the local value of the xy -component of the viscoelastic stress tensor $\boldsymbol{\sigma}$, and $\dot{\gamma}(y, t)$ is the local shear rate. Inserting Eq. (4) into Eq. (2) one sees that the xy -component of the total stress tensor \mathbf{T} has to be spatially constant, i.e. $\partial_y T = 0$. Therefore T can be only time-dependent. This implies

$$\begin{aligned} T(t) &= \langle \sigma(y, t) \rangle_y + \eta \langle \dot{\gamma}(y, t) \rangle_y \\ &= \bar{\sigma}(t) + \eta \bar{\gamma}(t), \end{aligned} \quad (5)$$

where $\langle A(y, t) \rangle_y = 1/L \int_0^L A(y, t) dy$ defines the spatial average over the y -direction of a quantity $A(y, t)$, which can be either the viscoelastic stress or the shear rate. Further, we have introduced the notation $\bar{A}(t) = \langle A(y, t) \rangle_y$.

In the present study we consider two rheological protocols: First, we impose a temporarily constant average shear rate $\bar{\dot{\gamma}}(t) = \bar{\dot{\gamma}} = \text{const.}$ to the system, yielding the local viscoelastic stress $\sigma(y, t)$ as the main dynamical variable. Using the force balance equation (4), the local shear rate $\dot{\gamma}(y, t)$ can then be calculated from

$$\dot{\gamma}(y, t) = \bar{\dot{\gamma}} + \frac{1}{\eta} [\bar{\sigma}(t) - \sigma(y, t)]. \quad (6)$$

Secondly, we impose a constant stress to the system, i.e., $T(t) = T^{\text{fix}} = \text{const.}$ From Eq. (5) it then follows that

$$\bar{\dot{\gamma}}(t) = \frac{1}{\eta} [T^{\text{fix}} - \bar{\sigma}(t)], \quad (7)$$

This already suggests that the stress controlled protocol ($T^{\text{fix}} = \text{const.}$) leads to a spatially homogeneous dynamics.

B. Model equations in the shear rate controlled protocol

In the present work we employ the rheological model proposed in Ref. [23], which couples the viscoelastic stress $\sigma(y, t)$ to a variable characterizing the microscopic structure. The latter is given by the length distribution $n(y, t)$ of elongated micelles.

The dynamics of $n(y, t)$ in the shear rate controlled protocol is governed by the non-linear relaxation equation

$$\partial_t n(y, t) = -\frac{n(y, t)}{\tau_n} + \frac{1}{\tau_n} \left(\frac{n_0}{1 + [\tau_n \dot{\gamma}(y, t)]^\beta} \right), \quad (8)$$

where τ_n is the relaxation time of the underlying rates of scission and recombination of the micelles, $n_0 > 0$ is the (average) length at zero shear and $\beta \geq 0$ is a power law exponent. While the first term on the right hand side of Eq. (8) is a pure relaxation term, the second term accounts for shear-induced changes of scission or recombination processes. The local shear rate $\dot{\gamma}(y, t)$ is determined through Eq. (6).

The homogeneous steady state solution ($\partial_t n(y, t) = 0$) of Eq. (8) reads

$$n_s(\bar{\dot{\gamma}}) = \frac{n_0}{1 + (\tau_n \bar{\dot{\gamma}})^\beta}. \quad (9)$$

In the low shear rate limit, $\bar{\dot{\gamma}} \rightarrow 0$, the steady state solution converges to n_0 , while in the limit of (infinitely) high shear rates ($\bar{\dot{\gamma}} \rightarrow \infty$) we find $n_s \rightarrow 0$. The rate

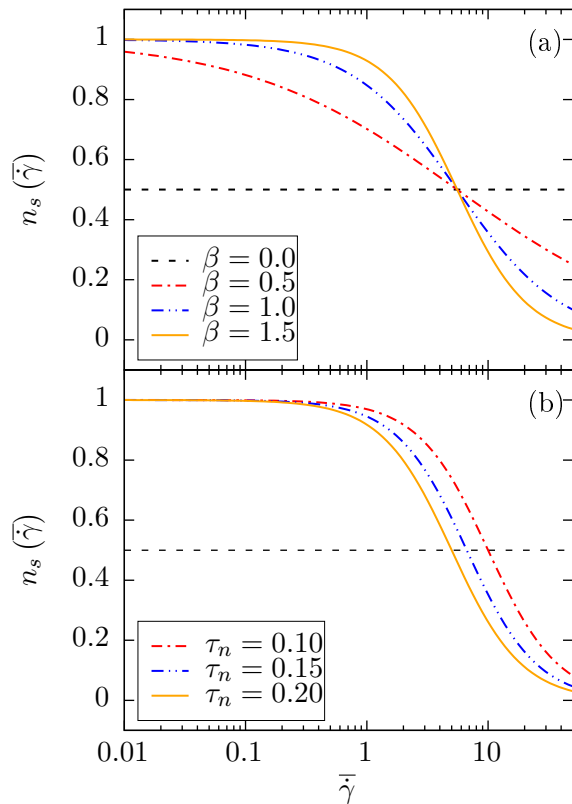


FIG. 1. Steady state solution n_s as function of the imposed shear rate $\bar{\dot{\gamma}}$ for (a) varying power law exponents β at $\tau_n = 0.180$ and (b) varying relaxation times τ_n at $\beta = 1.5$. The dashed horizontal line in (b) indicates where n_s is halved.

of convergence in this high shear rate limit strongly depends on the power law exponent β as illustrated in Fig. 1 (a). In the case $\beta = 0$ the steady state solution will be $n_s = n_0/2 = \text{const.}$ for all shear rates. The dependence of the function $n_s(\bar{\dot{\gamma}})$ on the relaxation time τ_n is shown in Fig. 1 (b). We further note that there is a critical shear rate $\bar{\dot{\gamma}}_c = \tau_n^{-1}$, at which the zero-shear length n_0 is halved upon increase of $\bar{\dot{\gamma}}$. Generally, the decrease of the micellar length with increasing shear rates reflects that scission processes become dominant. A similar behaviour has been observed in particle-based (Molecular Dynamics) computer simulations [38, 39]. Experimentally, the micellar length is hardly accessible.

The spatio-temporal dynamics of the viscoelastic stress $\sigma(y, t)$ is determined by the partial differential equation

$$\partial_t \sigma(y, t) = -\frac{\sigma(y, t)}{\tau(n)} + \frac{\dot{\gamma}(y, t)}{1 + [\tau(n) \dot{\gamma}(y, t)]^2} + \mathcal{D} \partial_y^2 \sigma(y, t), \quad (10)$$

with \mathcal{D} being the (stress-)diffusion constant and $\tau(n)$ a length dependent relaxation time [not to be confused with the time τ_n appearing in Eq. (8)]. The quantity

$\tau(n)$ is defined as

$$\tau(n) = \tau_0 \left(\frac{n(y,t)}{n_0} \right)^\alpha. \quad (11)$$

Here, $\tau_0 > 0$ is the zero-shear relaxation time of the micelles, and $\alpha \geq 0$ is another power law exponent. The homogeneous steady state solution ($\partial_t \sigma(y,t) = 0$) in the non-diffusive limit ($D = 0$) takes the following form:

$$\sigma_s(\bar{\gamma}) = \frac{\tau(n_s) \bar{\gamma}}{1 + (\tau(n_s) \bar{\gamma})^2}. \quad (12)$$

Here we have to distinguish several limiting cases: For $\alpha = 0$, the relaxation time reduces to a constant ($\tau(n_s) = \tau_0$), and therefore the coupling to the structural variable $n(y,t)$ vanishes. This case has been discussed, e.g., in Ref. [40]. The steady state solution σ_s is then equivalent to the steady state solution found for the xy -component of the viscoelastic stress tensor in the Johnson-Segalman model [41]. For $0 < \alpha < 1$, we find $\tau(n_s) > n_s$ for all shear rates. On the other hand, $\tau(n_s) < n_s$ for $\alpha > 1$ for all shear rates. Finally, in the special case $\alpha = 1$, the relaxation time follows instantaneously the micellar length, that is $\tau(n_s) \propto n_s$. The plausibility of the ansatz made in Eq. (11) is underlined by results from Molecular Dynamics simulations showing that the breaking time, which is similar to the relaxation time defined in Eq. (11), follows a power law like behaviour [42].

Using Eqs. (5) and (12) we can state an explicit expression for the total stress in the homogeneous stationary limit,

$$T_s(\bar{\gamma}) = \sigma_s(\bar{\gamma}) + \eta \bar{\gamma} = \frac{\tau(n_s) \bar{\gamma}}{1 + (\tau(n_s) \bar{\gamma})^2} + \eta \bar{\gamma}. \quad (13)$$

From the Johnson-Segalman model it is known that σ_s as function of $\bar{\gamma}$ displays a maximum at low shear rates and then converges towards zero for increasing shear rates. For the present model, the behaviour of σ_s as function of $\bar{\gamma}$ strongly depends on the choice of the power law exponent α : For $\alpha < 0.5$, we find the same behaviour as in the Johnson-Segalman model. However, for $\alpha \geq 0.5$ this behaviour changes such that the maximum at low shear rate is followed by two other extrema, that is one minimum and one maximum, before tending to zero at high shear rates. This non-monotonic behaviour reflects the highly non-linear character of the model equations (8) and (10). To get a more detailed insight into the impact of changing the relaxation time τ_n , which is attributed to scission and recombination processes, we plot in Fig. 2 the steady state solution of the total stress, $T_s(\bar{\gamma})$, for various τ_n . Upon increase of τ_n the maximum of the constitutive curve stays at the same position, while the minimum of the curve shifts to smaller shear rates. A further effect of increasing τ_n is a change of the slope of the high shear rate branch. This is again an indication for a stronger coupling to the (micro-)structure.

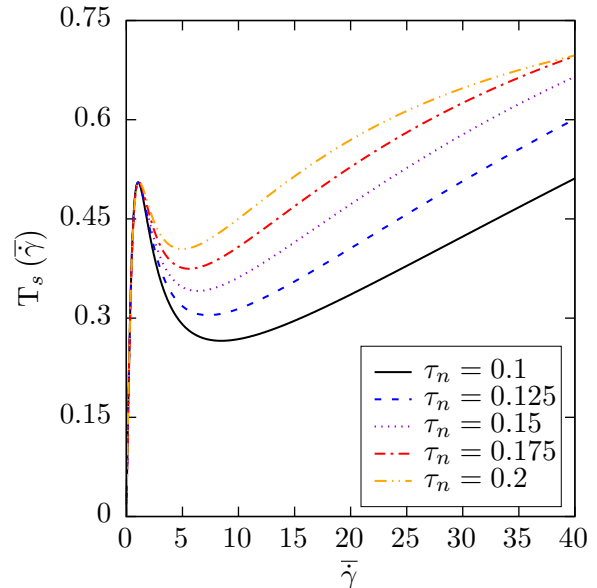


FIG. 2. Steady state solutions of the total stress for various relaxation times (fixed parameters: $\alpha = 1.2$, $\beta = 1.5$ and $\eta = 0.005$).

C. Model equations in the stress controlled protocol

The dynamical equations corresponding to the stress controlled protocol ($T(t) = T^{\text{fix}} = \text{const.}$) follow from Eqs. (8) and (10) by replacing the shear rate via Eq. (7), that is, $\bar{\gamma}(t) = 1/\eta [T^{\text{fix}} - \sigma(t)]$. This leads to

$$\partial_t \bar{n}(t) = -\frac{\bar{n}(t)}{\tau_n} + \frac{1}{\tau_n} \left(\frac{n_0}{1 + [\tau_n \eta^{-1} (T^{\text{fix}} - \sigma(t))]^\beta} \right) \quad (14)$$

and

$$\partial_t \bar{\sigma}(t) = -\frac{\bar{\sigma}(t)}{\tau(n)} + \frac{\eta^{-1} (T^{\text{fix}} - \sigma(t))}{1 + [\tau(n) \eta^{-1} (T^{\text{fix}} - \bar{\sigma}(t))]^2}, \quad (15)$$

with

$$\tau(\bar{n}) = \tau_0 \left(\frac{\bar{n}(t)}{n_0} \right)^\alpha. \quad (16)$$

III. LINEAR STABILITY ANALYSIS AND STATE DIAGRAMS

In order to get a first insight into the (complex) dynamics of our model system, we perform a linear stability analysis. We follow the strategy outlined in Ref. [43]. We then compare the results with those from a full numerical solution. As we will demonstrate, the overall dynamics strongly depends on the rheological protocol. We therefore discuss the two protocols separately.

A. Shear rate controlled protocol

1. Linear stability analysis

We start by introducing a two-dimensional vector containing the dynamical variables $n(y, t)$ and $\sigma(y, t)$,

$$\boldsymbol{\xi}(y, t) = \left[n(y, t), \sigma(y, t) \right]^T. \quad (17)$$

Within this vector notation we can rewrite Eqs. (5) and (10) as

$$\partial_t \boldsymbol{\xi}(y, t) = \mathbf{Q}(\boldsymbol{\xi}, \dot{\gamma}) + \partial_y^2 (\mathcal{D} \boldsymbol{\xi}(y, t)), \quad (18)$$

where $\mathbf{Q}(\boldsymbol{\xi}, \dot{\gamma})$ contains the non-linear terms on the r.h.s. of Eqs. (5) and (10). Further, we have introduced the diffusion matrix \mathcal{D} which is given by

$$\mathcal{D} = \begin{pmatrix} 0 & 0 \\ 0 & \mathcal{D} \end{pmatrix}. \quad (19)$$

The homogeneous steady state solutions of the dynamical system Eq. (18) are given in Eqs. (9) and (12), respectively. We summarize these solutions in a vector $\boldsymbol{\xi}_s = [n_s, \sigma_s]^T$. To determine whether $\boldsymbol{\xi}_s$ is stable or unstable, we add small heterogeneous perturbations $\delta \boldsymbol{\xi}(y, t)$, yielding

$$\boldsymbol{\xi}(y, t) = \boldsymbol{\xi}_s + \delta \boldsymbol{\xi}(y, t). \quad (20)$$

Due to the coupling between shear rate and viscoelastic stress given in Eq. (6), we additionally have to consider heterogeneous perturbations $\delta \dot{\gamma}(y, t)$ in the shear rate

$$\dot{\gamma}(y, t) = \bar{\gamma} + \delta \dot{\gamma}(y, t). \quad (21)$$

Substituting Eqs. (21) and (22) into Eq. (18) and linearising up to first order in the perturbations leads to

$$\begin{aligned} \partial_t \delta \boldsymbol{\xi}(y, t) = & \mathbf{M} \cdot \delta \boldsymbol{\xi}(y, t) + \mathbf{q} \cdot \delta \dot{\gamma}(y, t) \\ & + \partial_y^2 (\mathcal{D} \cdot \delta \boldsymbol{\xi}(y, t)), \end{aligned} \quad (22)$$

where $\mathbf{M} = \partial_{\boldsymbol{\xi}} \mathbf{Q}|_{\boldsymbol{\xi}_s, \bar{\gamma}}$ and $\mathbf{q} = \partial_{\dot{\gamma}} \mathbf{Q}|_{\boldsymbol{\xi}_s, \bar{\gamma}}$. To eliminate the perturbations in the shear rate we use the force balance equation (4), which in its linearised form is given by

$$0 = \mathbf{p} \cdot \delta \boldsymbol{\xi}(y, t) + \eta \delta \dot{\gamma}(y, t). \quad (23)$$

Here $\mathbf{p} = (0, 1)$ is a projection vector. Combining Eqs. (22) and (23) then yields

$$\partial_t \delta \boldsymbol{\xi}(y, t) = \left(\mathbf{J} + \partial_y^2 \mathcal{D} \right) \delta \boldsymbol{\xi}(y, t), \quad (24)$$

where \mathbf{J} is the Jacobian matrix given by

$$\mathbf{J} = \mathbf{M} - \frac{1}{\eta} \mathbf{q} \cdot \mathbf{p}. \quad (25)$$

real part	imag. part	character
$\mu_{1,2} < 0$	$\omega_{1,2} = 0$	stable fix point (sFP)
$\mu_{1,2} > 0$	$\omega_{1,2} = 0$	unstable fix point (uFP)
$\mu_1 > 0, \mu_2 < 0$	$\omega_{1,2} = 0$	unstable saddle (uSAD)
$\mu_{1,2} < 0$	$\omega_1 > 0, \omega_2 < 0$	stable focus (sFOC)
$\mu_{1,2} > 0$	$\omega_1 > 0, \omega_2 < 0$	unstable focus (uFOC)

TABLE I. Classification of the complex eigenvalues $\lambda = \mu + i\omega$ in the special case of a homogeneous system.

Explicit expressions for the elements of \mathbf{J} are given in Appendix A. We now assume the heterogeneous perturbations to be of exponential form such that

$$\delta \boldsymbol{\xi}(y, t) = \mathbf{C} e^{\lambda t + iky}, \quad (26)$$

where $\mathbf{C} = (C_1, C_2)^T$, $C_1, C_2 \in \mathbb{R}$, is an arbitrary constant vector, k is the wave number and $\lambda = \mu + i\omega$ is a complex number with $\mu, \omega \in \mathbb{R}$. The homogeneous steady state $\boldsymbol{\xi}_s$ is said to be stable, if $\mu < 0$, i.e., the perturbation dies out with time. Otherwise it is unstable. Inserting Eq. (26) into Eq. (24) leads to the eigenvalue problem

$$\det \left[\mathbf{J} - k^2 \mathcal{D} - \lambda \mathbf{I} \right] = 0. \quad (27)$$

From Eq. (27) it is seen that the complex eigenvalues λ depends on the wave number k and also on the imposed shear rate $\bar{\gamma}$ (via \mathbf{J}). To see the impact of k we plot in Fig. 3 the largest real part $\mu_{\max} = \mu_{\max}(k)$ (out of the two real parts of the two eigenvalues) at a fixed structural relaxation time τ_n and a fixed Newtonian viscosity η for three imposed shear rates $\bar{\gamma}$. In all cases, $\mu_{\max}(k)$ reaches its largest value at $k = 0$. For $k > 0$ the real part is a monotonic decaying function. This behaviour is a consequence of the asymmetric structure of Eq. (18) regarding the diffusion terms. As a result, the eigenvalue equation (27) contains only quadratic powers of k . The behaviour of $\mu_{\max}(k)$ indicates that the most unstable mode corresponds to $k = 0$. In the following we therefore restrict our attention to this mode alone. Physically, this restriction implies to consider the system as homogeneous, in other words, $\mathcal{D} = 0$.

The various stability scenarios occurring in this case can be classified according to table I. Investigating the complex eigenvalues for a range of (average) shear rates $\bar{\gamma}$ and relaxation times τ_n we obtain a stability diagram, which is presented in Fig. 4.

Below a critical point (CP) [44] the system shows essentially the same behaviour as the Johnson-Segalman model: There are two stable regions (stable fix point and stable focus), corresponding to homogeneous steady states, and one unstable region (unstable saddle). Within the Johnson-Segalman model the occurrence of the unstable saddle is associated with the regime, where the slope of the constitutive curve $T_s(\bar{\gamma})$ is negative, respectively where shear banding can occur [45]. Above the critical point the present system displays additionally

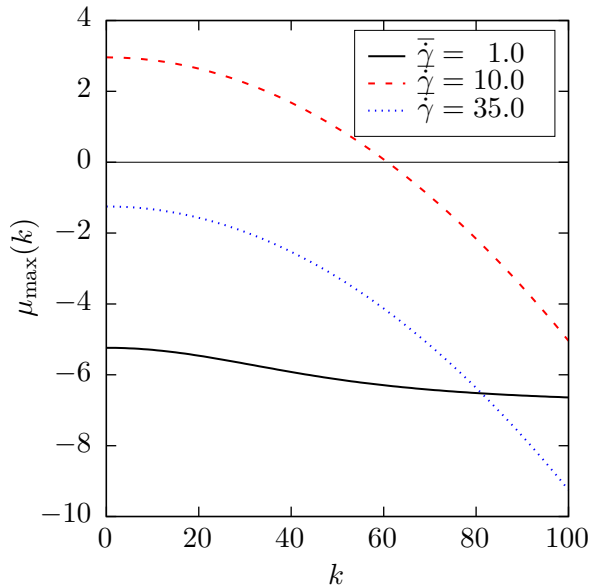


FIG. 3. Largest real part μ_{\max} of the complex eigenvalue λ as function of the wave number k for various imposed shear rates $\bar{\gamma}$ at fixed $\tau_n = 0.145$ and $\eta = 0.005$.

an unstable fix point and an unstable focus. The latter is separated from the stable focus by a Hopf bifurcation (corresponding to $\mu_{1,2} = 0$ and $\omega_1 > 0$, $\omega_2 < 0$). The Hopf bifurcation is absent in the Johnson-Segalman model and may thus be considered as a characteristic feature of the present model.

2. Numerical results

Our stability analysis at $k = 0$ clearly does not provide complete information on the system. To explore the full spatio-temporal dynamics at $\mathcal{D} \neq 0$ we solved Eqs. (8) and (10) numerically by using a Crank-Nicolson algorithm [46]. We sample over $N_t = 30,000$ temporal and $N_y = 150$ spatial discrete steps with a corresponding step size $dt = 0.005$ and $dy = 0.007$, yielding a total integration time of $T = N_t \cdot dt = 150$, and a gap size of $L = 1.0$. In analogy to Ref. [23], we fixed the two power law exponents at $\alpha = 1.2$ and $\beta = 1.5$, and the diffusion constant at $\mathcal{D} = 0.0016$. The equilibrium parameters, namely the zero-shear length and relaxation time, are set to $n_0 = \tau_0 = 1.0$, respectively. To ensure numerical stability we use the Courant-Friedrichs-Lewy criterion for forward time stepping given through $\sqrt{2\mathcal{D}dt} < dy$ [47]. To realize unique initial conditions for all numerical calculations, we prepared the stress to be homogeneous in space and the micellar length to be in a shear banded state given by $n(y, t = 0) = \bar{N} \cdot [1 + \Delta \cdot \cos(y\pi)]$. In order to check the sensitivity of the system with respect to the initial conditions, we varied the constants \bar{N} and Δ . The results presented here have been obtained with $\bar{N} = 0.5$ and $\Delta = 0.5$ corresponding to $\bar{n}(t = 0) = n_0/2$.

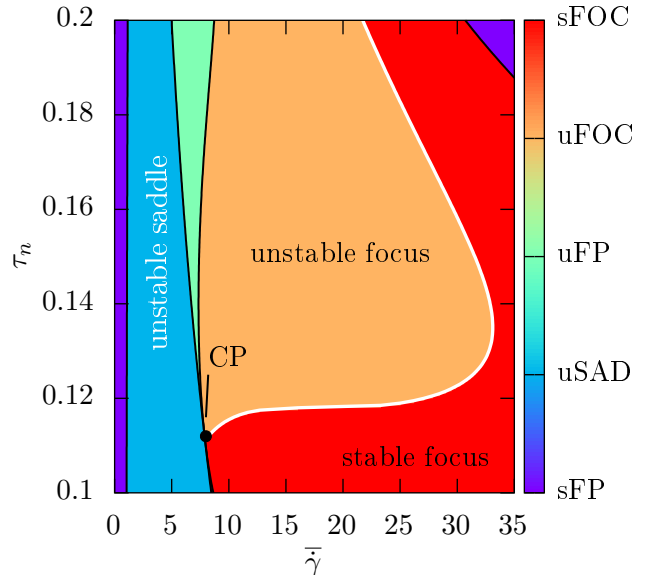


FIG. 4. Stability diagram obtained by solving the eigenvalue equation (26) for $k = 0$ in a range of relaxation times τ_n and imposed shear rates $\bar{\gamma}$. The states are classified according to table I. The Hopf bifurcation (solid white line) delimits the unstable and stable focus.

At the confining walls we employ Dirichlet boundary conditions through $\partial_y \sigma(y, t)|_{y=0} = 0$ and $\partial_y \sigma(y, t)|_{y=L} = 0$.

In our numerical calculations we performed “continuous shear ramps”. That is, starting from a given configuration of the dynamical variables, we solved the equations at constant $\bar{\gamma}$ up to the steady state limit, which is typically achieved at $T = 150$. To proceed towards the next (larger or smaller) value of the shear rate, we took the steady state configuration from the previous one as an initial configuration. By this strategy we are able to avoid stress “overshoots” in the start up regime of each shear step, leading to more stable numerical results. Further, this procedure is more realistic from an experimental point of view.

In Fig. 5 we present the state diagram for a ‘down’ ramp, that is starting from high shear rates and decreasing the shear rate step by step. It is seen that the system displays a variety of dynamical states, which differ from each other by the spatio-temporal behaviour of the viscoelastic stress $\sigma(y, t)$ and the other dynamical variables, that is, $n(y, t)$ and $\dot{\gamma}(y, t)$. We can distinguish six types of patterns (illustrated in Fig. 5): spatially homogeneous (h), (static) shear banding (sb), travelling pulses (tp), spatio-temporal oscillatory (o), mixture of spatio-temporal oscillatory and chaotic (oc) and purely chaotic in space and time (c). Some of the results have already been reported in Ref. [23] and in fact, our results are consistent with this earlier study. Here we have substantially extended the range of relaxation times τ_n and imposed shear rates $\bar{\gamma}$. In order to verify our classification made

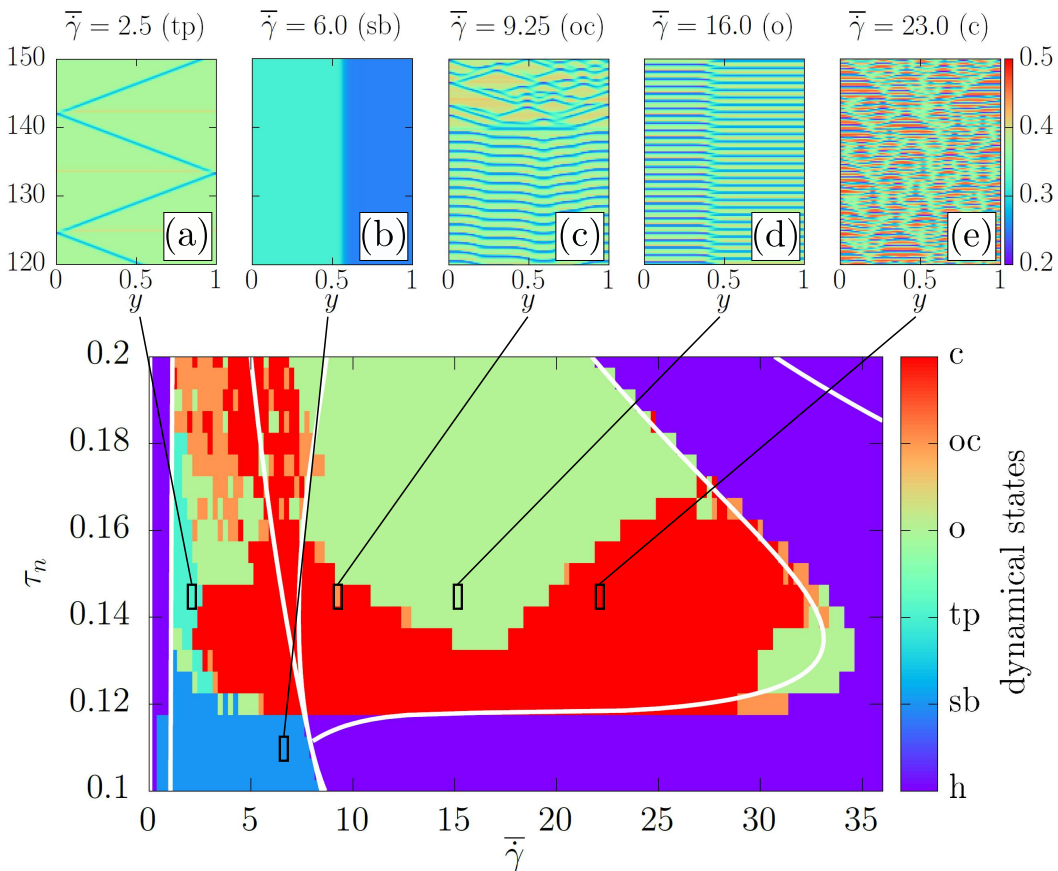


FIG. 5. Numerical results obtained at $\eta = 0.005$ and $\mathcal{D} = 0.0016$: The upper panel shows spatio-temporal patterns of the viscoelastic stress $\sigma(y, t)$ at different shear rates. These patterns correspond to (a) travelling pulses [tp], (b) shear banding [sb], (c) oscillatory-chaotic [oc], (d) oscillatory [o] and (e) chaotic [c] states. The lower panel shows the state diagram. The white lines result from the linear stability analysis.

for the dynamical states we also determined the largest Lyapunov exponent.

Inspecting the numerical results in Fig. 5 for small relaxation times $\tau_n \leq 0.112$, we see that the system behaves as predicted by linear stability analysis (and consistent with the Johnson-Segalman model). The regimes at low and high shear rates corresponding to homogeneous steady states are separated by a shear banded region associated with the unstable saddle. By increasing the relaxation time towards values above the critical point ($\tau_n > 0.112$), where the Hopf bifurcation arises, we enter a region rich of dynamical states, which have already been observed by Fielding and Olmsted [23]. In the subsequent discussion we especially focus on the purely oscillatory and chaotic states (as identified by the Lyapunov exponents), respectively.

Within the oscillatory state the system consists of a well defined high and low shear rate band, which change position periodically in time. Similar states have been observed experimentally [48–50]. In the present model the resulting oscillations of $\dot{\gamma}(y, t)$ are associated to oscillations of the micellar length $n(y, t)$. The time evolution of these quantities over one period as plotted in Fig. 6

(a) can be subdivided into four stages:

- (i) At very low local shear rate, the micellar length is maximal. From a physical point of view this corresponds to a situation, where the system consists of isotropically distributed and entangled micelles.
- (ii) The local shear rate starts to increase, while the micellar length decreases: This can be interpreted such that the micellar network starts to break down (due to increasing shear forces), while the micelles align in the shear flow.
- (iii) The local shear rate reaches its maximum, whereas the micellar length is found to be minimal: In this case the shear forces are so large that scission processes are dominating, yielding particularly small values of the micellar length.
- (iv) At the end of the cycle the local shear rate is still quite high but so is the degree of alignment of the micelles. Therefore, end-end-recombination processes are more likely to happen, and the micelles start to grow again.

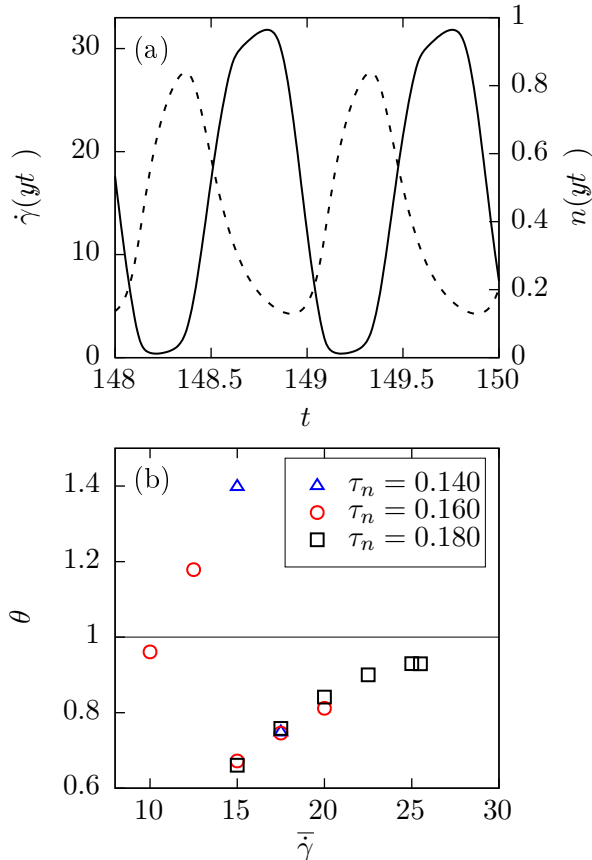


FIG. 6. (a) Temporal evolution of the local shear rate $\dot{\gamma}(y, t)$ (solid line) and the micellar length $n(y, t)$ (dashed line) at $y = 0.8$ for $\bar{\gamma} = 16.0$ and $\tau_n = 0.145$. (b) Frequency ratio θ for the oscillatory states within the unstable focus determined from power spectra at three relaxation times τ_n (fixed parameters: $\eta = 0.005$, $\mathcal{D} = 0.0016$, $\alpha = 1.2$ and $\beta = 1.5$).

To quantify the oscillatory dynamics inside the unstable regime we extract the fundamental frequency f^* from a time series of the total stress $T(t)$ [see Eq. (5)] by creating a power spectrum. We then compare f^* to the frequency $f = \omega/(2\pi)$ obtained from linear stability analysis by introducing the ratio $\theta = f/f^*$. Numerical results for θ are shown in Fig. 6 (b).

Inspecting the frequency ratio θ for the oscillatory and chaotic states, we find that for low and moderate relaxation times, i.e. $\tau_n = 0.140$ and $\tau_n = 0.160$, no clear trend is visible. For high relaxation times, here $\tau_n = 0.180$, the system reveals only oscillatory states. Generally, we find the linear stability results underestimates the frequency for the total investigated shear rate range. Especially at the lower bound of the unstable focus the numerically determined frequency is about a factor 2.5 higher than the estimated one. We recall, however, that the linear stability analysis is restricted to homogeneous states, therefore, deviations are expected. Interestingly, close to the Hopf bifurcation the numeri-

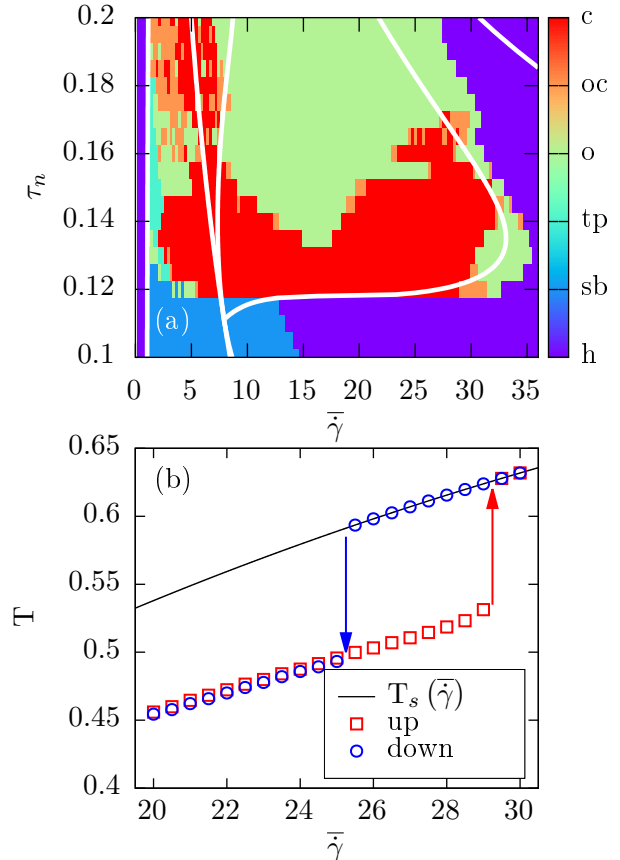


FIG. 7. (a) State diagram for the ‘up’ ramp revealing the same dynamical states as classified in Fig. 5. (b) Total stress T as function of the imposed shear rate $\bar{\gamma}$ at $\tau_n = 0.180$ as given by the analytical steady state solution (solid line, Eq. (13)) and the numerical data for the up and down ramp (fixed parameters: $\eta = 0.005$, $\mathcal{D} = 0.0016$, $\alpha = 1.2$ and $\beta = 1.5$).

cal and analytical results match quite well. These results already give hints where it is possible to manipulate the dynamics of the system using time-delayed feedback control.

So far we have been focusing on the ‘down’ ramp. The corresponding state diagram for an ‘up’ ramp (i.e. increasing $\bar{\gamma}$ from low values) is presented in Fig. 7 (a). Comparing the two state diagrams in Figs. 5 and 7 (a) at low relaxation times, i.e. below the critical point (where only shear banded states exist) we conclude that the system reveals the same hysteric behaviour, which was already described for the Johnson-Segalman model elsewhere [51]. However, comparing the state diagrams above the critical point, we find for the up ramp the oscillatory region to be extended towards higher shear rates. To clarify this point, we plot in Fig. 7 (b) numerical steady state results for the total stress for the two ramp protocols. While for the ‘down’ ramp the numerical data leave the analytical steady state solution [see Eq. (13)] ex-

actly at the Hopf bifurcation, the corresponding data for the ‘up’ protocol remains below the analytical one even after crossing the predicted Hopf bifurcation. This indicates that the system reveals a second instability, which is not covered by our linear stability analysis.

B. Stress controlled protocol

For the linear stability analysis of the stress controlled protocol we follow the same procedure outlined in the previous section. A simplification arises through the fact that now the dynamical variables are only be time-dependent. At first, we define the vector $\boldsymbol{\xi}(t) = [n(t), \sigma(t)]^T$ containing the dynamical variables of the system. Within this vector notation Eqs. (14) and (15) can be written as

$$\partial_t \boldsymbol{\xi}(t) = \mathbf{Q}(\boldsymbol{\xi}, T^{\text{fix}}), \quad (28)$$

where $\mathbf{Q}(\boldsymbol{\xi}, T^{\text{fix}})$ summarizes the right hand sides of the two dynamical equations. We recall here that, unlike in the shear rate controlled protocol, the total stress is set to a constant. Further, we introduce the vector $\boldsymbol{\xi}_s = [n_s, \sigma_s]^T$ containing the steady state solutions of the dynamical system [see Eq. (28)]. To determine the stability of these steady states, we add small time-dependent perturbations $\delta\boldsymbol{\xi}(t)$ to $\boldsymbol{\xi}_s$

$$\boldsymbol{\xi}(t) = \boldsymbol{\xi}_s + \delta\boldsymbol{\xi}(t) = \boldsymbol{\xi}_s + \mathbf{C} e^{\lambda t}, \quad (29)$$

with $\mathbf{C} = (C_1, C_2)^T$ being a constant vector with $C_1, C_2 \in \mathbb{R}$ and $\lambda = \mu + i\omega$, $\mu, \omega \in \mathbb{R}$, being the complex eigenvalue. Inserting this ansatz into Eq. (28) and linearising up to first order in the perturbations leads to the eigenvalue problem

$$\det[\mathbf{J} - \lambda \mathbf{I}] = 0. \quad (30)$$

Here $\mathbf{J} = \partial_{\boldsymbol{\xi}} \mathbf{Q}|_{\boldsymbol{\xi}_s, T^{\text{fix}}}$ is the Jacobian matrix of the dynamical system, which is explicitly derived in Appendix B. When solving the eigenvalue equation (30) we find a quite simple stability diagram, see Fig. 8, (compared to the shear rate controlled protocol). It reveals a stable fix point (homogeneous steady state), an unstable focus (homogeneous oscillatory state) delimited by a Hopf bifurcation, and a stable focus (homogeneous steady state). The transition between the region of stable fix points and unstable focus is characterised by hysteretic behaviour (bistability). This reduced complexity compared to Fig. 4 is a consequence of the fact that within the stress controlled protocol, there are only time-dependent states, such that the dimensionality of the system is reduced to $d = 2$. This excludes to observe any chaotic states, since chaos requires dimension $d \geq 3$ [52].

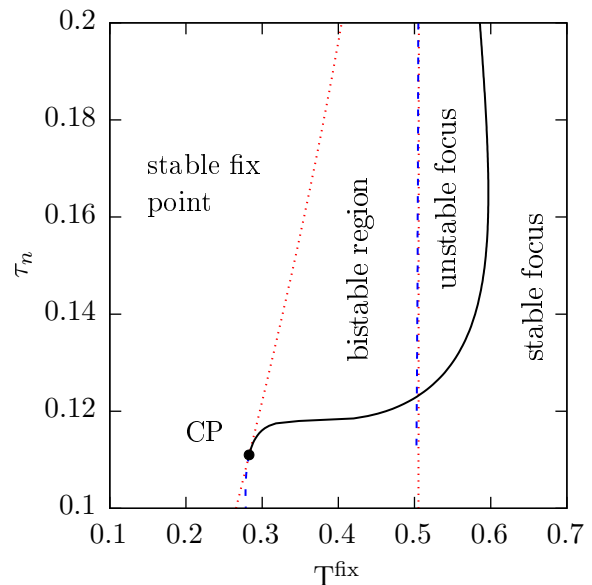


FIG. 8. Stability diagram for the stress controlled protocol obtained by solving the eigenvalue equation (30) in a range of relaxation times τ_n (fixed parameters: $\alpha = 1.2$, $\beta = 1.5$, $\eta = 0.005$).

IV. FEEDBACK CONTROL

In this section we discuss the application of time-delayed feedback control (TDFC) to our model system with the primary goal being to suppress oscillatory and chaotic states in favour of steady states. This is particularly motivated by an experimental study, where TDFC was used to control chaotic states appearing in Taylor-Couette flow of a complex fluid [34]. As control protocol we here use the Pyragas scheme [29], where the control term is built of the (local) difference $\xi(y, t) - \xi(y, t - \tau)$ of the dynamical variable ξ at the present time t and an earlier time $t - \tau$ with τ being the delay time. Within this section we discuss two approaches how to implement Pyragas control to our model system. First, we apply the TDFC to both dynamical variables, yielding a diagonal control scheme. Second, we use the control term only in the dynamical equation for the viscoelastic stress (non-diagonal control). As we will show, the results are surprisingly similar.

A. Diagonal control scheme

In the case of diagonal control we add a Pyragas-like term to the equations of both variables, $n(y, t)$ and $\sigma(y, t)$. This choice is motivated by earlier studies on the application of TDFC to systems under shear [36, 53, 54]. Our general goal is to stabilize a steady state $\boldsymbol{\xi}_s = [n_s, \sigma_s]^T$ within the parameter range of the unstable focus, which we determined in the Sec. III A 1 by using

linear stability analysis. We note here that the diagonal control scheme is, in our system, somewhat unphysical. The reason is that the micellar length is experimentally hardly accessible, therefore it seems impossible to “feed” this variable back into the system. Here we still consider this scheme due to its simplicity.

Within the vector notation introduced in Sec. III A, the dynamics of the shear rate controlled protocol with Pyragas control is of the form

$$\begin{aligned} \partial_t \boldsymbol{\xi}(y, t) &= \mathbf{Q}(\boldsymbol{\xi}, \dot{\gamma}) + \partial_y^2 (\mathcal{D} \boldsymbol{\xi}(y, t)) \\ &+ K \left[\boldsymbol{\xi}(y, t) - \boldsymbol{\xi}(y, t - \tau) \right], \end{aligned} \quad (31)$$

where K is the control strength and τ is the delay time. In order to get some insight into the effect of TDFC on the dynamics we perform linear stability analysis of the delayed differential equation, following the steps outlined in Ref. [55]. We start by adding small heterogeneous perturbations $\delta \boldsymbol{\xi}(y, t)$ and $\delta \dot{\gamma}(y, t)$ to the steady states $\boldsymbol{\xi}_s$ and the imposed shear rate $\dot{\gamma}$, respectively. Inserting these perturbations in Eq. (31) and linearising up to first order we obtain

$$\begin{aligned} \partial_t \delta \boldsymbol{\xi}(y, t) &= \left(\mathbf{J} + \partial_y^2 \mathcal{D} - K \mathbf{I} \right) \delta \boldsymbol{\xi}(y, t) \\ &+ K \delta \boldsymbol{\xi}(y, t - \tau). \end{aligned} \quad (32)$$

Here, \mathbf{J} is the Jacobian matrix derived in Eq. (25) for the uncontrolled system (see also Appendix A). We describe the perturbations as $\delta \boldsymbol{\xi}(y, t) = \mathbf{C} e^{\nu t + iky}$, where $\mathbf{C} = (C_1, C_2)^T$ is an arbitrary constant vector and $\nu = \mu' + i\omega'$ is the ‘controlled’ complex eigenvalue ($\mu', \omega' \in \mathbb{R}$). Inserting this ansatz into Eq. (32) leads to the eigenvalue problem

$$\det \left[\mathbf{J} - k^2 \mathcal{D} - (\nu + K (1 - e^{-\nu \tau})) \mathbf{I} \right] = 0. \quad (33)$$

Comparing the eigenvalue problem defined in Eq. (33) with the uncontrolled one given in Eq. (27), we find them to be of the same functional form. Consequently, the eigenfunctions $\delta \boldsymbol{\xi}(y, t)$ are the same for both scenarios. Therefore, if the ‘uncontrolled’ complex eigenvalues λ are known, it is possible to determine the controlled eigenvalues ν through

$$\lambda = \nu + K (1 - e^{-\nu \tau}). \quad (34)$$

For convenience we dropped here the dependency of the eigenvalues on the wave number k . We rearrange Eq. (34) and multiply both sides of the resulting equation by the delay time τ to reach

$$(\nu + K - \lambda) \tau = K \tau e^{-\nu \tau}. \quad (35)$$

In this equation we identify $z = (\nu + K - \lambda) \tau$ on the left hand side. Multiplying both sides of Eq. (36) by e^z leads to

$$z e^z = K \tau e^{(K-\lambda)\tau}. \quad (36)$$

To solve Eq. (36) for the eigenvalue ν we employ the Lambert- \mathcal{W} -function [56]. For any complex number $z \in \mathbb{C}$, the Lambert- \mathcal{W} -function is the inverse of the function $f(z) = z e^z$ such that

$$z = f^{-1}(z e^z) = \mathcal{W}(z e^z). \quad (37)$$

Re-substituting the expression for z we identified before we obtain an expression for the “controlled” eigenvalue ν depending on the “uncontrolled” eigenvalue λ ,

$$\nu = \frac{1}{\tau} \mathcal{W} \left(K \tau e^{(K-\lambda)\tau} \right) + \lambda - K. \quad (38)$$

Here $\nu = \nu(k)$ as well as $\lambda = \lambda(k)$ depend on k .

The control scheme is considered to be successful, if $\text{Re}(\nu) < 0$. We thus define $\text{Re}(\nu) = 0$ to be the criterion for “neutral” stability, respectively the neutral stability borders. In a previous study [55] of Pyragas control of oscillatory states (close to the Hopf bifurcation), it has been demonstrated, that the minimal control strength K_{\min} required for stabilization is given by

$$K_{\min} = \frac{\mu}{2}. \quad (39)$$

The corresponding delay time is determined through

$$\tau_j = \left(\frac{2j+1}{2} \right) T_0, \quad (40)$$

where $T_0 = (2\pi)/\text{Im}(\lambda) = (2\pi)/\omega$ is the oscillation period obtained from the stability analysis of the uncontrolled case, and $j \in \mathbb{N}_0$. Further, it has been shown that the neutral stability curves in the τ - K -plane are given by

$$\tau_c(K) = \begin{cases} \frac{\pm \arccos((K - \mu)/K) + 2j\pi}{\omega \mp \sqrt{\mu(2K - \mu)}}, & \text{for } \left| \frac{K - \mu}{K} \right| \leq 1 \\ \text{not defined,} & \text{else.} \end{cases} \quad (41)$$

Here, $j \in \mathbb{Z}$. In Fig. 9 (a) we present the stability borders at an exemplary shear rate $\dot{\gamma}$ and relaxation time τ_n for several wave numbers k . Like in the uncontrolled case discussed in Sec. III A 1 we find the most unstable mode at $k = 0$ and therefore we will stick to this mode for the subsequent discussion. In order to visualize the impact of $\dot{\gamma}$, we plot Fig. 9 (b) the stability borders for several shear rates. With increasing $\dot{\gamma}$ we observe the minima of the stability curves to be shifted towards smaller delay times. Further, the width of the stability domains is increasing.

The results we presented so far are obtained from analytical calculations in the framework of linear stability analysis, but this does not provide information on the impact of TDFC on the spatio-temporal behaviour of our model system. Therefore we have additionally solved the dynamical system (31) using a Crank-Nicolson algorithm. To determine whether the system reaches a homogeneous steady state, we calculate the largest Lyapunov exponent Λ_{\max} from the time series of the total stress $\mathbf{T}(t)$ using

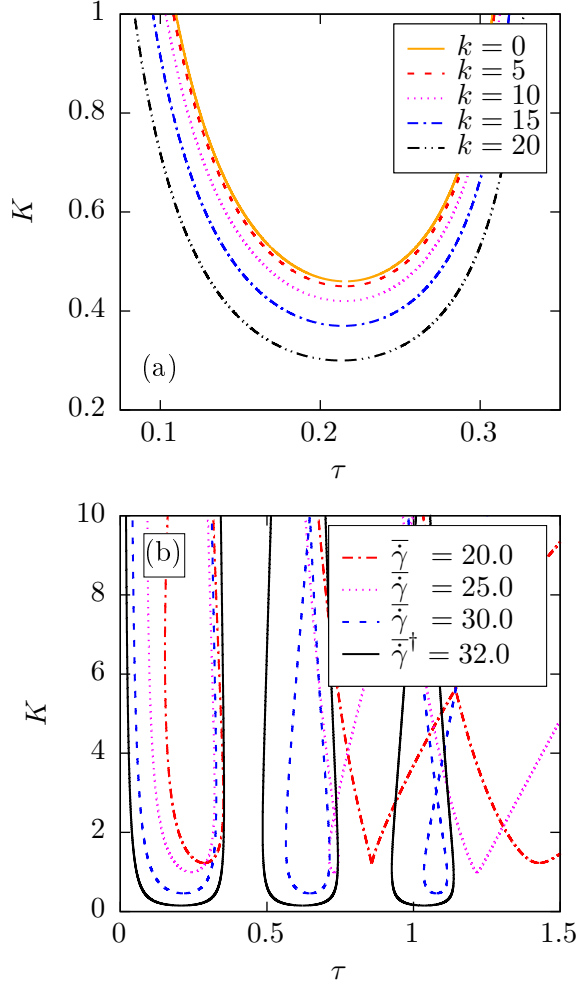


FIG. 9. (a) Stability borders for different wave numbers k as functions of the delay time τ (at fixed $\bar{\gamma} = 30.0$ and $\tau_n = 0.140$) and (b) neutral stability curves for $k = 0$ at fixed $\tau_n = 0.140$ for various shear rates. The dagger marks a shear rate close to the Hopf bifurcation.

the Wolf-algorithm [57]. A comparison of analytical and numerical results is presented in Fig. 10 for a moderate relaxation time $\tau_n = 0.140$ and an imposed shear rate $\bar{\gamma} = 32.0$ close to the Hopf bifurcation, which corresponds to a purely oscillatory state (see state diagram Fig. 5).

It is seen that the control is successful in the sense, that Λ_{\max} is negative within the stability borders, indicating that the system indeed reaches a homogeneous steady state. In contrast, $\Lambda_{\max} > 0$ outside the stability domains. We thus conclude that the results from the full numerical solution are consistent with those from the

(linear) stability analysis.

B. Non-diagonal control scheme

So far we have investigated the impact of time-delayed feedback control applied to both dynamical variables, $n(y, t)$ and $\sigma(y, t)$. Now we turn our attention to the scenario, where the control term is applied only to one dynamical variable, namely the viscoelastic stress $\sigma(y, t)$. This choice is motivated, first, by the fact that it is experimentally just not feasible to feed back the local micellar length. A second argument in favour of this “non-diagonal” scheme is, that the viscoelastic stress is coupled directly to the local shear rate, which represents the true experimental variable to be controlled. The functional form of the control term is chosen to be again of a Pyragas-type [29].

In our vectorial notation, the dynamical equation for this scenario is given by

$$\begin{aligned} \partial_t \boldsymbol{\xi}(y, t) = & \mathbf{Q}(\boldsymbol{\xi}, \dot{\gamma}) + \partial_y^2 (\mathcal{D} \boldsymbol{\xi}(y, t)) \\ & - K \mathbf{A} [\boldsymbol{\xi}(y, t) - \boldsymbol{\xi}(y, t - \tau)], \end{aligned} \quad (42)$$

where \mathbf{A} is a non-diagonal 2×2 matrix defined by

$$\mathbf{A} = \begin{pmatrix} 0 & 0 \\ 0 & 1 \end{pmatrix} \quad (43)$$

This form ensures that the control is only applied to $\sigma(y, t)$. We note that a similar scheme has been proposed by Kyrychko and co-workers for the one-species control in the Gray-Scott model [32], which belongs to the class of reaction-diffusion systems.

We start again by deriving analytic expressions for the controlled eigenvalues $\nu = \mu' + i\omega'$ in the framework of linear stability analysis, following the procedure outlined for the uncontrolled case in Sec. III A 1. Assuming heterogeneous perturbations $\delta \boldsymbol{\xi}(y, t)$ and $\delta \dot{\gamma}(y, t)$, substituting these perturbations into Eq. (42) and linearising up to first order leads to

$$\begin{aligned} \partial_t \delta \boldsymbol{\xi}(y, t) = & \left(\mathbf{J} + \partial_y^2 \mathcal{D} - K \mathbf{A} \right) \delta \boldsymbol{\xi}(y, t) \\ & + K \mathbf{A} \delta \boldsymbol{\xi}(y, t - \tau). \end{aligned} \quad (44)$$

This result is similar to Eq. (32) for the diagonal control scheme. In the present case, the eigenvalue problem takes the form (with $\delta \boldsymbol{\xi}(y, t) = \mathbf{C} e^{\nu t + iky}$)

$$\begin{vmatrix} J_{11} - \nu & J_{12} \\ J_{21} & J_{22} - k^2 \mathcal{D} - K(1 - e^{-\nu\tau}) - \nu \end{vmatrix} = 0, \quad (45)$$

where J_{ij} ($i, j = 1, 2$) are the components of the Jacobian matrix given in Eq. (25). Calculating the determinant, Eq. (45) can be rewritten as

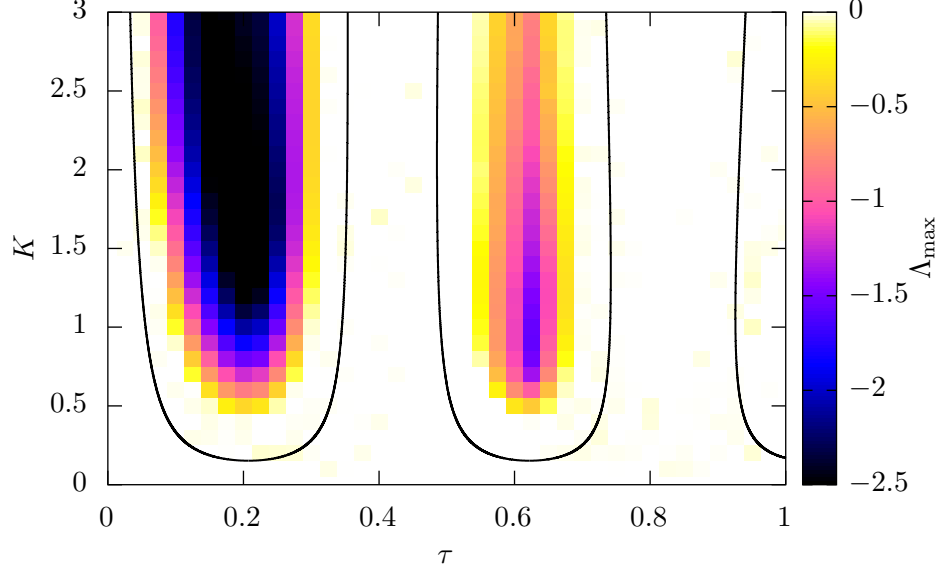


FIG. 10. Largest Lyapunov exponent Λ_{\max} determined from numerically solving Eq. (31) for $\tau_n = 0.140$ and $\bar{\gamma} = 32.0$ (fixed parameters: $\alpha = 1.2$, $\beta = 1.5$, $\eta = 0.005$, $\mathcal{D} = 0.0016$).

$$\nu^2 + \nu \left\{ -K (e^{-\nu\tau} - 1) + k^2 \mathcal{D} - (J_{11} + J_{22}) \right\} + \left\{ J_{11} \left[K (e^{-\nu\tau} - 1) - k^2 \mathcal{D} \right] + J_{11} J_{22} - J_{12} J_{21} \right\} = 0. \quad (46)$$

In principle, we have to distinguish here again between two cases, namely $k = 0$ and $k > 0$. However, we have shown in the previous section, the most unstable mode occurs at $k = 0$. Thus we consider only the latter case, yielding

$$\nu^2 + \nu \left\{ -K (e^{-\nu\tau} - 1) - A \right\} + \left\{ J_{11} K (e^{-\nu\tau} - 1) + B \right\} = 0, \quad (47)$$

with $A = J_{11} + J_{22}$ and $B = J_{11} J_{22} - J_{12} J_{21}$. This

equation can not be solved via the Lambert- \mathcal{W} -function.

To simplify the analysis we consider a state close to the Hopf bifurcation, where the real μ' part of the eigenvalue ν is approximately zero and thus, $\nu = i\omega'$ is purely imaginary. Substituting this assumption into Eq. (47) leads to

$$-\omega'^2 + i\omega' \left[-K (e^{-i\omega'\tau} - 1) - A \right] + \left[J_{11} K (e^{-i\omega'\tau} - 1) + B \right] = 0. \quad (48)$$

Separating Eq. (48) into real and imaginary part yields

$$-\omega'^2 + K \left[J_{11} \cos(\omega'\tau) - \omega' \sin(\omega'\tau) - J_{11} \right] + B = 0, \quad (49)$$

$$-\omega' A + K \left[-\omega' \cos(\omega'\tau) - J_{11} \sin(\omega'\tau) + \omega' \right] = 0. \quad (50)$$

Solving Eqs. (49) and (50) yields a pair of solutions (τ, K) , which depend on the imaginary part ω' of the

eigenvalue ν . Specifically, the delay time $\tau = \tau(\omega')$ is given by

$$\tau(\omega') = \frac{1}{\omega'} \left[\arctan \left(\frac{2\omega' (A J_{11} - B + \omega'^2) (B J_{11} + (A - J_{11}) \omega'^2)}{(B J_{11})^2 - C_1 \omega'^2 + C_2 \omega'^4 - \omega'^6} \right) + 2j\pi \right], \quad j \in \mathbb{Z} \quad (51)$$

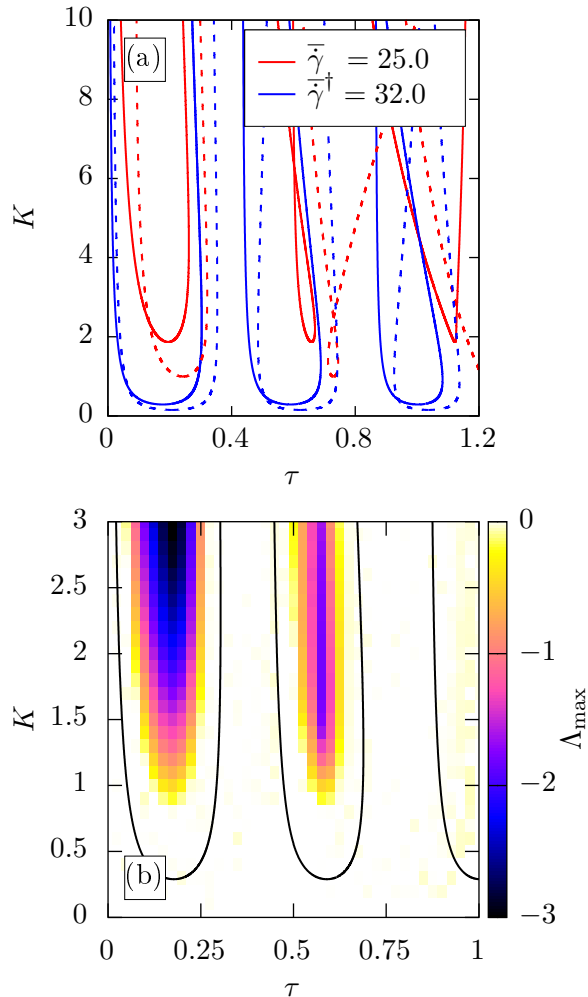


FIG. 11. (a) Stability curves at fixed $\tau_n = 0.140$ at two imposed shear rates $\bar{\gamma}$ for the diagonal control scheme (dashed lines) and the non-diagonal control scheme (solid lines) and (b) largest Lyapunov exponent Λ_{\max} determined from numerics at fixed $\tau_n = 0.140$ and $\bar{\gamma} = 30.0$; the dagger marks the shear rate close to the Hopf bifurcation.

with $C_1 = B^2 + (AJ_{11})^2 + 2BJ_{11}(J_{11} - 2A)$ and $C_2 = A^2 - 2B - 4AJ_{11} + J_{11}^2$. These two constants depend on the system parameters α , β , τ_n , η and $\bar{\gamma}$. Further, the argument of the arctangent in Eq. (51) is by definition limited to the interval $[-\pi/2, +\pi/2]$. The control strength $K = K(\omega')$ follows as

$$K(\omega') = \frac{(A\omega')^2 + (\omega'^2 - B)^2}{2(BJ_{11} + \omega'^2(A - J_{11}))}. \quad (52)$$

These results are similar to the ones derived in Ref. [32] for the Gray-Scott model.

Due to the highly non-linear structure of Eqs. (51) and (52) it is impossible to derive analytic expressions for the minimal control strength K_{\min} . We thus focus on the neutral stability curves defined by $\nu = \mu' = 0$.

In Fig. 11 (a) we plot these curves for both, the non-diagonal and diagonal control scheme. It is seen that the location (in parameter space) and shape of the curves is quite similar. Comparing the two situations in more detail, we find that the minima of the stability curves of the non-diagonal scheme are shifted towards smaller delay times τ and higher control strengths K . This shift gets even more pronounced when choosing a shear rate far away from the Hopf bifurcation such as $\bar{\gamma} = 25.0$ for $\tau_n = 0.140$. However, overall the results from the simpler diagonal control scheme provide a good estimate for the non-diagonal case. In order to determine the impact of the non-diagonal control scheme on the spatio-temporal dynamics, we plot in Fig. 11 (b) the largest Lyapunov exponent Λ_{\max} , (determined from the time series of the total stress $T(t)$ using the Wolf-algorithm [57]). Again, the numerical results are consistent with those from stability analysis at $k = 0$.

V. CONCLUSIONS

In this publication we have applied time-delayed feedback control (specifically, the Pyragas scheme) to manipulate the complex dynamics of a solution of wormlike micelles based on a non-local rheological model proposed by Fielding and Olmsted [23]. As a background we have performed a linear stability analysis (at $k = 0$) for uncontrolled systems at constant (average) shear rate, as well as systems at constant total stress. Further, we solved the dynamical system numerically to get an insight into the full spatio-temporal behaviour for a broad range of parameters. In doing this, we considered both an “up” ramp, i.e. increasing the shear from low values, and a “down” ramp, that is, decreasing the shear rate from high values. Comparing the corresponding numerical results with the analytical predictions from linear stability analysis (at $k = 0$), we find a good agreement of the data for the “down” ramp. For the “up” ramp, the system displays hysteric behaviour not captured by the linear stability analysis. This hysteresis effect has already been observed in the Johnson-Segalman model [51] within the bistable region related to shear banding. In the model investigated here, the hysteresis occurs near the Hopf bifurcation located at the high shear rate branch of the constitutive curve.

We have then investigated the changes of the dynamics upon application of Pyragas control [29]. For the case of the diagonal Pyragas scheme (where both variables are controlled on the same footing), we have derived analytic expressions for the neutral stability curves delimiting the stability domains in the plane spanned by the control strength, K , and the delay time, τ . Within these domains the control is successful in the sense that the resulting state is a stable steady state. From a physical point of view, however, the diagonal control scheme is not feasible, since the micellar length is experimentally hardly accessible. We therefore additionally explored a

non-diagonal control scheme, where the control term is only applied to the viscoelastic stress. Comparing the two approaches (diagonal and non-diagonal control) we find the stability domains are indeed rather similar (for the non-diagonal case, they are somewhat shifted towards smaller delay times and higher control strengths). This shows that the (theoretically simpler) diagonal scheme can serve as a rough estimate of the other case.

Clearly, it would be very interesting to test the implications of our feedback control (or related schemes) experimentally. One possibility to implement control would be via adaptive protocols within the experimental set-up, e.g., a rheometer. We also mention recent progress in accessing the spatio-temporal structure of micellar solutions under shear using appropriate scattering techniques (Rheo-SANS) [58, 59]. Given these developments, an application of TDFC to avoid or stabilize certain shear-induced behaviors seems very promising.

ACKNOWLEDGMENTS

We gratefully acknowledge financial support from the Deutsche Forschungsgemeinschaft (DFG) through project B2 within the Collaborative Research Center 910. The authors thank Michael Gradzielski for the fruitful discussions and the input from the experimental point of view.

Appendix A: Jacobian matrix for the shear rate controlled protocol

We start from the compact notation for the dynamical system given in Eq. (18) in Sec. III A 1

$$\partial_t \boldsymbol{\xi}(y, t) = \mathbf{Q}(\boldsymbol{\xi}, \dot{\gamma}) + \partial_y^2 (\mathcal{D} \boldsymbol{\xi}(y, t)) , \quad (\text{A1})$$

where \mathcal{D} is the diffusion matrix and the vector $\mathbf{Q}(\boldsymbol{\xi}, \dot{\gamma})$ follows from Eq. (8) and (10)

$$\begin{aligned} \mathbf{Q}(\boldsymbol{\xi}, \dot{\gamma}) &= \begin{pmatrix} -\frac{n(y,t)}{\tau_n} + \frac{1}{\tau_n} \left(\frac{n_0}{1+(\tau_n \dot{\gamma}(y,t))^\beta} \right) \\ -\frac{\sigma(y,t)}{\tau(n)} + \frac{\dot{\gamma}(y,t)}{1+(\tau(n) \dot{\gamma}(y,t))^2} \end{pmatrix} \\ &= \begin{pmatrix} Q_1(n, \sigma, \dot{\gamma}) \\ Q_2(n, \sigma, \dot{\gamma}) \end{pmatrix} . \end{aligned} \quad (\text{A2})$$

The Jacobian matrix \mathbf{J} for the shear rate controlled protocol is defined by

$$\mathbf{J} = \mathbf{M} - \frac{1}{\eta} \mathbf{q} \cdot \mathbf{p} , \quad (\text{A3})$$

with $\mathbf{M} = \partial_{\boldsymbol{\xi}} \mathbf{Q}|_{\boldsymbol{\xi}_s, \bar{\gamma}}$ and $\mathbf{q} = \partial_{\dot{\gamma}} \mathbf{Q}|_{\boldsymbol{\xi}_s, \bar{\gamma}}$. We first consider the matrix \mathbf{M} . The latter can be written in terms of the components of the vector \mathbf{Q}

$$\mathbf{M} = \partial_{\boldsymbol{\xi}} \mathbf{Q}|_{\boldsymbol{\xi}_s, \bar{\gamma}} = \begin{pmatrix} \partial_n Q_1 & \partial_\sigma Q_1 \\ \partial_n Q_2 & \partial_\sigma Q_2 \end{pmatrix} \Big|_{\boldsymbol{\xi}_s, \bar{\gamma}} . \quad (\text{A4})$$

Inserting the expressions for $Q_1(n, \sigma, \dot{\gamma})$ and $Q_2(n, \sigma, \dot{\gamma})$ given in Eq. (A2) and evaluating the derivatives at the steady state values one obtains

$$\partial_n Q_1(n, \sigma, \dot{\gamma})|_{\boldsymbol{\xi}_s, \bar{\gamma}} = -\frac{1}{\tau_n} \quad (\text{A5})$$

$$\partial_\sigma Q_1(n, \sigma, \dot{\gamma})|_{\boldsymbol{\xi}_s, \bar{\gamma}} = 0 \quad (\text{A6})$$

$$\partial_n Q_2(n, \sigma, \dot{\gamma})|_{\boldsymbol{\xi}_s, \bar{\gamma}} = \frac{\alpha \sigma_s}{n_s^{\alpha+1}} - \frac{2\alpha \bar{\gamma}^3 n_s^{2\alpha-1}}{\left[1 + (\bar{\gamma} n_s^\alpha)^2\right]^2} \quad (\text{A7})$$

$$\partial_\sigma Q_2(n, \sigma, \dot{\gamma})|_{\boldsymbol{\xi}_s, \bar{\gamma}} = -\frac{1}{n_s^\alpha} . \quad (\text{A8})$$

Second, we consider the vector \mathbf{q} ,

$$\mathbf{q} = \partial_{\dot{\gamma}} \mathbf{Q}|_{\boldsymbol{\xi}_s, \bar{\gamma}} = \begin{pmatrix} \partial_{\dot{\gamma}} Q_1 \\ \partial_{\dot{\gamma}} Q_2 \end{pmatrix} \Big|_{\boldsymbol{\xi}_s, \bar{\gamma}} . \quad (\text{A9})$$

Using Eq. (A2) we obtain

$$\partial_{\dot{\gamma}} Q_1(n, \sigma, \dot{\gamma})|_{\boldsymbol{\xi}_s, \bar{\gamma}} = -\frac{\beta (\tau_n \bar{\gamma})^\beta}{\tau_n \bar{\gamma} \left[1 + (\tau_n \bar{\gamma})^\beta\right]^2} , \quad (\text{A10})$$

$$\partial_{\dot{\gamma}} Q_2(n, \sigma, \dot{\gamma})|_{\boldsymbol{\xi}_s, \bar{\gamma}} = \frac{1 - (\bar{\gamma} n_s^\alpha)^2}{\left[1 + (\bar{\gamma} n_s^\alpha)^2\right]^2} . \quad (\text{A11})$$

Inserting the elements of \mathbf{M} and \mathbf{q} into Eq. (A3) for the matrix \mathbf{J} , one finds the following elements J_{ij} ($i, j = 1, 2$)

$$J_{11} = -\frac{1}{\tau_n} \quad (\text{A12})$$

$$J_{12} = \frac{\beta (\tau_n \bar{\gamma})^\beta}{\eta \tau_n \bar{\gamma} \left[1 + (\tau_n \bar{\gamma})^\beta\right]^2} \quad (\text{A13})$$

$$J_{21} = \frac{\alpha \sigma_s}{n_s^{\alpha+1}} - \frac{2\alpha \bar{\gamma}^3 n_s^{2\alpha-1}}{\left[1 + (\bar{\gamma} n_s^\alpha)^2\right]^2} \quad (\text{A14})$$

$$J_{22} = -\frac{1}{n_s^\alpha} - \frac{1 - (\bar{\gamma} n_s^\alpha)^2}{\eta \left[1 + (\bar{\gamma} n_s^\alpha)^2\right]^2} . \quad (\text{A15})$$

For convenience we set $n_0 = \tau_0 = 1.0$ for all calculations.

Appendix B: Jacobian matrix for the stress controlled protocol

In the stress controlled protocol the shear rate is replaced by $\bar{\gamma}(t) = 1/\eta [\text{T}^{\text{fix}} - \bar{\sigma}(t)]$, with T^{fix} being a constant. In vector notation the dynamical system can be written

$$\partial_t \boldsymbol{\xi}(t) = \mathbf{Q}(\boldsymbol{\xi}(t)) , \quad (\text{B1})$$

where the vector $\mathbf{Q}(\boldsymbol{\xi}(t))$ is given by

$$\begin{aligned} \mathbf{Q}(\boldsymbol{\xi}(t)) &= \begin{pmatrix} -\frac{n(t)}{\tau_n} + \frac{1}{\tau_n} \left(\frac{n_0}{1+(\tau_n/\eta) [\mathbf{T}^{\text{fix}} - \sigma(t)]^\beta} \right) \\ -\frac{\sigma(t)}{\tau(n(t))} + \frac{1/\eta [\mathbf{T}^{\text{fix}} - \sigma(t)]}{1+[\tau(n(t))/\eta] [\mathbf{T}^{\text{fix}} - \sigma(t)]^2} \end{pmatrix} \\ &= \begin{pmatrix} Q_1(n(t), \sigma(t)) \\ Q_2(n(t), \sigma(t)) \end{pmatrix}. \end{aligned} \quad (\text{B2})$$

The Jacobian matrix \mathbf{J} evaluated at the steady state values can be written as

$$\mathbf{J} = \partial_{\boldsymbol{\xi}} \mathbf{Q} \Big|_{\boldsymbol{\xi}_s, \mathbf{T}^{\text{fix}}} = \begin{pmatrix} \partial_n Q_1 & \partial_\sigma Q_1 \\ \partial_n Q_2 & \partial_\sigma Q_2 \end{pmatrix} \Big|_{\boldsymbol{\xi}_s, \mathbf{T}^{\text{fix}}}. \quad (\text{B3})$$

Explicitly, the components J_{ij} ($i, j = 1, 2$) of the Jacobian matrix are given by

$$J_{11} = -\frac{1}{\tau_n} \quad (\text{B4})$$

$$J_{12} = \frac{\beta [\tau_n/\eta (\mathbf{T}^{\text{fix}} - \sigma_s)]^{\beta-1}}{\eta \left[1 + (\tau_n/\eta (\mathbf{T}^{\text{fix}} - \sigma_s))^\beta \right]^2} \quad (\text{B5})$$

$$J_{21} = \frac{\alpha}{n_s^{\alpha+1}} \left[\sigma_s + \frac{2\eta (n_s^\alpha (\mathbf{T}^{\text{fix}} - \sigma_s))^3}{\left[\eta^2 + (n_s^\alpha (\mathbf{T}^{\text{fix}} - \sigma_s))^2 \right]^2} \right] \quad (\text{B6})$$

$$J_{22} = -\frac{1}{n_s^\alpha} + \frac{\eta \left[(n_s^\alpha (\mathbf{T}^{\text{fix}} - \sigma_s))^2 - \eta^2 \right]}{\left[(n_s^\alpha (\mathbf{T}^{\text{fix}} - \sigma_s))^2 + \eta^2 \right]^2}. \quad (\text{B7})$$

For convenience we set $n_0 = \tau_0 = 1.0$ for all calculations.

-
- [1] P. D. Olmsted, O. Radulescu, and C.-Y. D. Lu, *J. Rheol.* **44**, 257 (2000).
[2] S. M. Fielding, *Soft Matter* **3**, 1262 (2007).
[3] P. D. Olmsted, *Rheol. Acta* **47**, 283 (2008).
[4] T. Divoux, M. A. Fardin, S. Manneville, and S. Lerouge, *Annu. Rev. Fluid Mech.* **48**, 81 (2016).
[5] M. W. Johnson and D. Segalman, *J. Nonnewton. Fluid Mech.* **2**, 255 (1977).
[6] J.-F. Berret, in *Molecular Gels*, edited by R. G. Weiss and P. Terech (Springer, Dordrecht, 2006), p. 667.
[7] M. E. Cates and S. M. Fielding, *Adv. Phys.* **55**, 799 (2006).
[8] C. A. Dreiss, *Soft Matter* **3**, 956 (2007).
[9] S. Lerouge and J.-F. Berret, *Adv. Polym. Sci.* **230**, 1 (2010).
[10] J. Yang, *Curr. Opin. Colloid Interface Sci.* **7**, 276 (2002).
[11] P. Sullivan, E. B. Nelson, V. Anderson, and T. Hughes, *Surfactant Science Series* **140**, 453 (2007).
[12] I. Wunderlich, H. Hoffmann, and H. Rehage, *Rheol. Acta* **26**, 532 (1987).
[13] H. Rehage and H. Hoffmann, *J. Phys. Chem.* **92**, 4712 (1988).
[14] M. E. Cates and M. S. Turner, *Europhys. Lett.* **11**, 681 (1990).
[15] M. S. Turner and M. E. Cates, *Langmuir* **7**, 1590 (1991).
[16] J.-B. Salmon, A. Colin, and D. C. Roux, *Phys. Rev. E* **66**, 031505 (2002).
[17] R. Ganapathy and A. K. Sood, *Phys. Rev. Lett.* **96**, 108301 (2006).
[18] R. Ganapathy and A. K. Sood, *Langmuir* **22**, 11016 (2006).
[19] R. Ganapathy and A. K. Sood, *J. Nonnewton. Fluid Mech.* **149**, 78 (2008).
[20] M. E. Cates, D. A. Head, and A. Ajdari, *Phys. Rev. E* **66**, 025202 (2002).
[21] D. A. Head, A. Ajdari, and M. E. Cates, *Europhys. Lett.* **57**, 120 (2002).
[22] S. M. Fielding and P. D. Olmsted, *Eur. Phys. J. E* **11**, 65 (2003).
[23] S. M. Fielding and P. D. Olmsted, *Phys. Rev. Lett.* **92**, 084502 (2004).
[24] A. Aradian and M. E. Cates, *Europhys. Lett.* **70**, 397 (2005).
[25] G. Rienäcker, M. Kröger, and S. Hess, *Physica A* **315**, 537 (2002).
[26] G. Rienäcker, M. Kröger, and S. Hess, *Phys. Rev. E* **66**, 040702 (2002).
[27] B. Chakrabarti, M. Das, C. Dasgupta, S. Ramaswamy, and A. K. Sood, *Phys. Rev. Lett.* **92**, 055501 (2004).
[28] M. Das, B. Chakrabarti, C. Dasgupta, S. Ramaswamy, and A. K. Sood, *Phys. Rev. E* **71**, 021707 (2005).
[29] K. Pyragas, *Phys. Lett. A* **170**, 421 (1992).
[30] E. Schöll and H. G. Schuster, eds., *Handbook of Chaos Control* (Wiley VCH, Weinheim, 2008).
[31] E. Schöll, S. H. L. Klapp, and P. Hövel, eds., *Control of Self-Organizing Nonlinear Systems* (Springer, Berlin,

- 2016).
- [32] Y. N. Kyrychko, K. B. Blyuss, S. J. Hogan, and E. Schöll, *Chaos* **19**, 043126 (2009).
- [33] S. V. Gurevich and R. Friedrich, *Phys. Rev. Lett.* **110**, 014101 (2013).
- [34] O. Lüthje, S. Wolff, and G. Pfister, *Phys. Rev. Lett.* **86**, 1745 (2001).
- [35] M. Zeitz, P. Gurevich, and H. Stark, *Eur. Phys. J. E* **38**, 22 (2015).
- [36] D. A. Strehober, E. Schöll, and S. H. L. Klapp, *Phys. Rev. E* **88**, 062509 (2013).
- [37] R. G. Larson, *The Structure and Rheology of Complex Fluids* (Oxford University Press Inc., 1999).
- [38] M. Kröger and R. Makhloufi, *Phys. Rev. E* **53**, 2531 (1996).
- [39] J. T. Padding, E. S. Boek, and W. J. Briels, *J. Chem. Phys.* **129**, 074903 (2008).
- [40] N. A. Spenley, X. F. Yuan, and M. E. Cates, *J. Phys. II* **6**, 551 (1996).
- [41] D. S. Malkus, J. A. Nohel, and B. J. Plohr, *J. Comput. Phys.* **87**, 464 (1990).
- [42] J. T. Padding and E. S. Boek, *EPL (Europhysics Lett.)* **66**, 756 (2004).
- [43] R. L. Moorcroft and S. M. Fielding, *J. Rheol.* **58**, 103 (2014).
- [44] A more detailed numerical investigation (MATCONT) reveals that this critical point is a Bogdanov-Takens point.
- [45] P. Espanol, X. F. Yuan, and R. C. Ball, *J. Nonnewton. Fluid Mech.* **65**, 93 (1996).
- [46] W. H. Press, S. A. Teukolsky, W. T. Vetterling, and b. P. Flannery, *Numerical Recipes in C: The Art of Scientific Computing* (Cambridge University Press, 2002), 2nd ed.
- [47] R. Courant, K. Friedrichs, and H. Lewy, *Math. Ann.* **100**, 32 (1928).
- [48] H. Azzouzi, J. P. Decruppe, S. Lerouge, and O. Greffier, *Eur. Phys. J. E* **17**, 507 (2005).
- [49] S. Lerouge, M.-A. Fardin, M. Argentina, G. Grégoire, and O. Cardoso, *Soft Matter* **4**, 1808 (2008).
- [50] M.-A. Fardin, T. Divoux, M. A. Guedeau-Boudeville, I. Buchet-Maulien, J. Browaeys, G. H. McKinley, S. Manneville, and S. Lerouge, *Soft Matter* **8**, 2535 (2012).
- [51] J. M. Adams, S. M. Fielding, and P. D. Olmsted, *J. Nonnewton. Fluid Mech.* **151**, 101 (2008).
- [52] S. H. Strogatz, *Nonlinear dynamics and chaos: with applications to physics, biology, chemistry, and engineering* (Westview Press, 1994), 1st ed.
- [53] D. A. Strehober, H. Engel, and S. H. L. Klapp, *Phys. Rev. E* **88**, 012505 (2013).
- [54] M. Zeitz, P. Gurevich, and H. Stark, *Eur. Phys. J. E* **38**, 22 (2015).
- [55] P. Hövel and E. Schöll, *Phys. Rev. E* **72**, 046203 (2005).
- [56] R. M. Corless, G. H. Gonnet, D. E. G. Hare, D. J. Jeffrey, and D. E. Knuth, *Adv. Comput. Math.* **5**, 329 (1996).
- [57] A. Wolf, J. B. Swift, H. L. Swinney, and J. A. Vastano, *Physica D* **16**, 285 (1985).
- [58] M. E. Helgeson, M. D. Reichert, Y. T. Hu, and N. J. Wagner, *Soft Matter* **5**, 3858 (2009).
- [59] C. R. López-Barrón, A. K. Gurnon, A. P. R. Eberle, L. Porcar, and N. J. Wagner, *Phys. Rev. E* **89**, 042301 (2014).